

A General Cyanine-Based Platform for Designing Robust Dual-Channel Near-Infrared Fluorescent and Photoacoustic Probes

Pingzhou Wu, Zheng Qu, Jie Zhang,* Xiaojie Ren, Dongqing Wang, Chen Huang, Ke Cheng, Junyang Qi, Heng Shi, Shenglong Gan, Wenyu Wei, Yachao Zhang, Chun-Sing Lee, Lidai Wang,* and Hongyan Sun*

The creation of versatile platforms for developing dual-channel near-infrared fluorescent (NIRF) and photoacoustic (PA) probes, especially those engineered to minimize channel crosstalk, is crucial for precise biomarker detection. However, such platforms remain scarce. To bridge this gap, this study introduces an innovative cyanine-based platform, CySN. The CySN platform showcases remarkable wavelength-shifting properties, including large fluorescent modality shift (68 nm) and PA modality shift (145 nm) after the decaging reaction. These substantial changes lead to an exceptionally high ratiometric NIRF change of 603-fold and ratiometric PA change of 261-fold. Leveraging the CySN platform, dual-channel NIRF/PA probes have been successfully developed for detecting both small molecule biomarker (H_2O_2) and enzyme biomarker (esterase). These probes demonstrate the ability to detect their targets through dual-channel NIRF/PA detection with high sensitivity and selectivity *in vitro*. Furthermore, the probes effectively harness NIRF signals to image target analytes in living cells. Notably, the probes demonstrate the capability to accurately diagnose tumors by detecting tumor markers (H_2O_2 and esterase), revealing a 3.6 to 7-fold ratiometric PA enhancement over normal tissue. Therefore, the CySN platform holds the potential to further advance the development of dual-channel NIRF/PA probes for biomolecule detection in disease diagnosis.

1. Introduction

Molecular imaging provides a powerful approach for studying the mechanism of biomolecules in various biological processes and advances medical diagnosis through real-time and noninvasive detection.^[1] Near-infrared fluorescent (NIRF) and photoacoustic (PA) dual-modal imaging, harnessing the advantages of high sensitivity in fluorescent modality and deep imaging depth in PA modality, has emerged as a valuable method for *in vivo* molecular imaging.^[2] For instance, Pu and coworkers developed several renal-clearable NIRF/PA dual-modal probes that are particularly appealing for detecting biomarkers associated with various diseases.^[3] In terms of probe design, activatable probes demonstrated superior signal specificity and signal-to-background ratio (SBR) compared with the “always on” probes.^[4] Furthermore, the incorporation of a dual-channel response can provide self-calibration function, which can minimize false positives and thereby enhances detection accuracy.^[5]

P. Wu, J. Zhang, X. Ren, D. Wang, C. Huang, S. Gan, W. Wei, C.-S. Lee,
 H. Sun
 Department of Chemistry and COSDAF
 (Center of Super-Diamond and Advanced Films)
 City University of Hong Kong
 83 Tat Chee Avenue, Kowloon, Hong Kong 999077, China
 E-mail: jzhan35-c@my.cityu.edu.hk; hongysun@cityu.edu.hk

Z. Qu, L. Wang
 Department of Biomedical Engineering
 City University of Hong Kong
 83 Tat Chee Avenue, Kowloon, Hong Kong 999077, China
 E-mail: lidawang@cityu.edu.hk

J. Zhang, H. Shi
 Center for Regenerative Medicine and Health
 Hong Kong Institute of Science and Innovation
 Chinese Academy of Sciences
 Hong Kong 999077, China

D. Wang
 Sichuan Provincial Key Laboratory for Human Disease Gene Study and the
 Center for Medical Genetics
 Department of Laboratory Medicine
 Sichuan Academy of Medical Sciences & Sichuan Provincial People's
 Hospital University of Electronic Science and Technology of China
 Chengdu 610072, China

 The ORCID identification number(s) for the author(s) of this article can be found under <https://doi.org/10.1002/adfm.202400597>
 © 2024 The Authors. Advanced Functional Materials published by Wiley-VCH GmbH. This is an open access article under the terms of the Creative Commons Attribution-NonCommercial-NoDerivs License, which permits use and distribution in any medium, provided the original work is properly cited, the use is non-commercial and no modifications or adaptations are made.

DOI: 10.1002/adfm.202400597

Nevertheless, there is a scarcity of activatable dual-channel NIRF/PA probes, underscoring the urgent need for general platforms that meet the requisite properties.

Currently, the majority of existing activatable NIRF/PA probes are designed based on a single-channel “turn-on” strategy.^[4a,c] The probes with a single-channel read-out are susceptible to false signals arising from variations in probe concentration. Although significant progress has been achieved in mitigating interferences through the development of NIRF/PA probes with a ratiometric mode, many of these probes exhibit ratiometric properties in only one modality or are limited to specific target detections.^[6,7] This lack of universality prevents them from serving as versatile platforms for constructing NIRF/PA probes.

Recently, hemicyanine fluorophores have become important templates for constructing smart NIRF probes.^[8] Furthermore, sulfur-substituted hemicyanine dyes have emerged as promising scaffolds for dual ratiometric NIRF/PA applications.^[9] However, the signals from the two channels of NIRF/PA modality exhibit a relatively large overlay in the scaffold, adversely affecting the sensitivity of the ratiometric read-out (Figure 1a). Therefore, the development of general platforms with minimal channel crosstalk, capable of producing sensitive and reliable ratiometric signal outputs, is imperative for the further advancement of activatable dual-channel NIRF/PA probes.

Cyanine dyes, well-known for their superior fluorescence quantum yield, high absorption coefficient and excellent biocompatibility, have become the most important class of NIR fluorophores for bioimaging.^[10] Notably, indocyanine green (ICG)^[11] and IRDye-800CW^[12] from this class have found extensive use in clinical trials. Herein, we present a general cyanine-based platform **CySN** for creating activatable high-contrast dual-channel NIRF/PA probes. As depicted in Figure 1b, **CySN** platform consists of three parts: (1) a recognition group for biomarker detection; (2) a sulfur-substituted cyanine that produces the initial signals of NIRF₈₁₂ and PA₇₈₀; (3) a conjugation linker that can undergo self-immolation after decaging reaction with biomarkers. This decaging reaction yields amine-substituted cyanine with distinctive signals of NIRF₇₄₄ and PA₆₃₅. Excitingly, the model reaction revealed that the channel crosstalk in both NIRF and PA modes in **CySN** platform is significantly lower compared to the reported scaffolds, resulting in one to two magnitudes higher ratiometric changes for NIRF

(F₇₄₄/F₈₁₂) and PA (PA₆₃₅/PA₇₈₀). To underscore its universality, we extended the application of **CySN** platform to develop dual-channel NIRF/PA probes for H₂O₂ (a small molecule biomarker for tumor) and esterase (an enzyme biomarker for tumor). Both probes exhibit robust target detection through high-contrast ratiometric NIRF/PA output. Importantly, these probes demonstrate a high tumor-to-normal tissue ratio of 3.6

to 7 with ratiometric PA detection, affirming their precision in *in vivo* detection.

2. Results and Discussion

2.1. Design and Model Experiments of Dual-Channel NIRF/PA Platform

We hypothesized that cyanine-based IR-780 analog is well-suited for constructing the aimed platform because: 1) its long wavelength is conducive for *in vivo* imaging; 2) the absorption, fluorescence and PA signal of cyanine dyes can be modified by different donors (S, N, O); 3) there is a balanced distribution of energy transformation between the dye’s NIRF and PA signals; 4) cyanine-based fluorophores show high potential for clinical transformation. On the other hand, the thermodynamic stability of C–S bond is lower than that of C–N bond at physiological condition (pH = 7.4). In cyanine dyes, the NH group is prone to attacking the S atom in the nearby C–S bond. This process eventually leads to the formation of a more stable C–N bond.^[13] As a result, we developed the **CySN** platform, a sulfur-substituted cyanine integrated with a cysteamine linker, which is caged by a recognition group. When the target triggers the decaging reaction, **CySN** undergoes 1,6-elimination, followed by a Smiles rearrangement. Consequently, both the NIRF and PA signals of the probe undergo a significant blue shift, providing a distinctive ratiometric readout.

To assess the suitability of **CySN** platform for dual-channel NIRF/PA response, we initially synthesized **CySN-Boc** (Scheme S1, Supporting Information) and conducted a model experiment. As depicted in Figure 2a, the Boc group of **CySN-Boc** could be removed by TFA to form the intermediate **CySN-NH₃⁺**. In an acidic buffer (pH = 2), the protonated NH group does not replace the S group and exhibit its initial signal. In a neutral buffer (pH = 7.4), the NH group will attack the S group, leading to the generation of **Cy-NS**. This transformation will cause a significant blue shift in both the absorption and emission of **CySN-NH₃⁺**.

As shown in Figure 2c, following deprotection with TFA, **CySN-NH₃⁺** itself exhibited a high emission peak at 812 nm. As anticipated, in neutral environment, the fluorescence emission peak of **CySN-NH₃⁺** at 812 nm significantly decreased, accompanied by the emergence of a new peak at 744 nm due to the donor exchanging from S to N. (Figure 2b,c). Moreover, both the absorption and PA signals of **CySN-NH₃⁺** shifted from 780 nm to 635 nm, respectively, after transitioning from an acidic environment to a neutral environment (Figure 2d,e). Furthermore, we evaluated the photophysical properties of **CySN-Boc** and **Cy-NS** (Table S1, Supporting Information). The results demonstrated **CySN-Boc** and **Cy-NS** exhibited high extinction coefficients (>10⁴ M⁻¹ cm⁻¹) and suitable quantum yields, supporting that **CySN** has balanced fluorescence and PA output and the ability of dual-channel NIRF/PA response.

Next, we conducted a more in-depth quantitative analysis of the dual-channel NIRF/PA properties of **CySN** platform using the model experiment. As shown in Figure 3a, **CySN** platform exhibited a 68 nm wavelength shift in the fluorescent modality and 145 nm wavelength shift in the PA modality after transition from **CySN-Boc** to **CyNS**. The wavelength shift in fluorescent/PA modality of **CySN** platform was 1.7/2.4-fold higher

K. Cheng, J. Qi
School of Pharmaceutical Sciences (Shenzhen)
Shenzhen Campus of Sun Yat-sen University
Shenzhen 518107, China

Y. Zhang
Suzhou Institute of Biomedical Engineering and Technology
Chinese Academy of Sciences
Suzhou, Jiangsu 215163, China

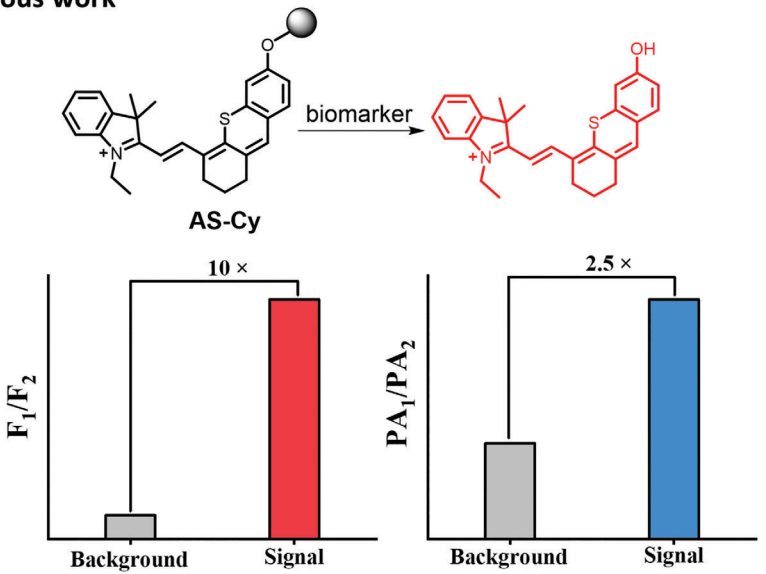
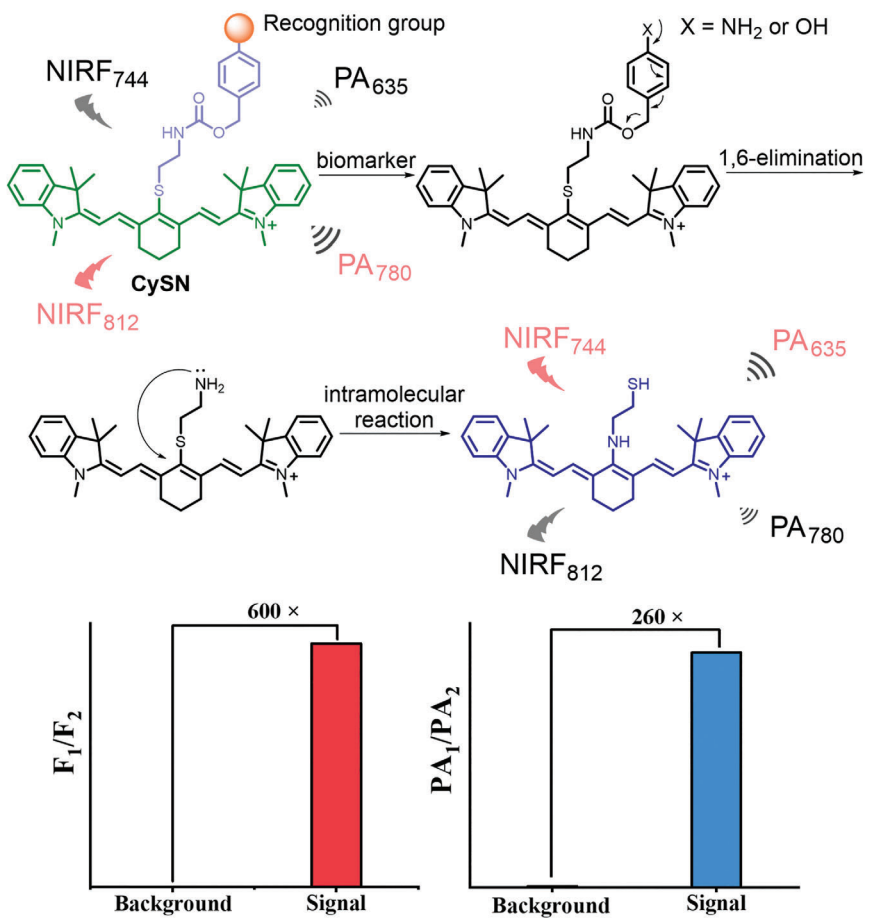
a Previous work**b This work**

Figure 1. a) Previous work on ratiometric NIRF/PA probes utilizing AS-Cy and their corresponding signal outputs. b) Schematic illustration of the design strategy, response mechanism and signal output of our dual-channel NIRF/PA CySN platform in this study.

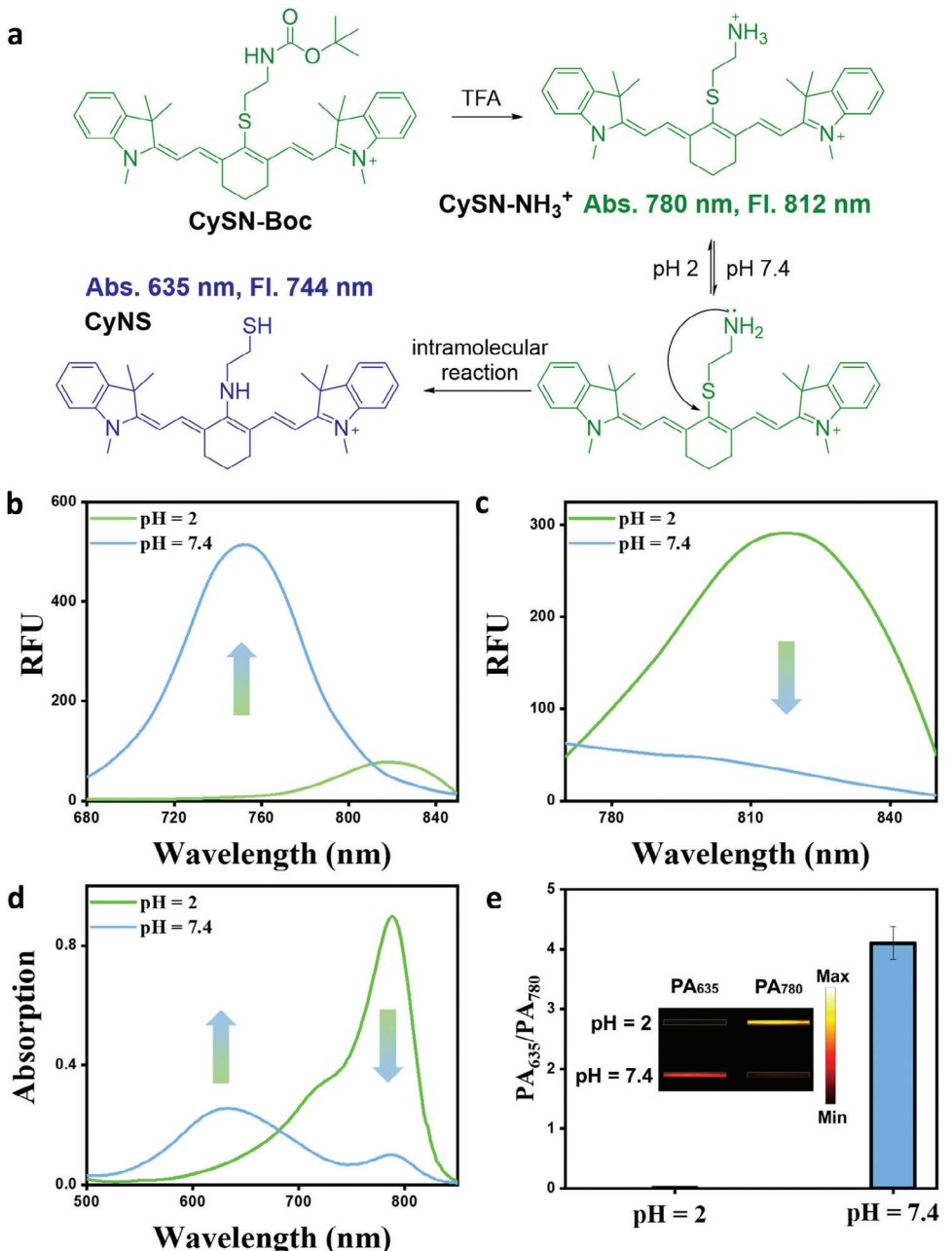


Figure 2. a) Schematic illustration of the response mechanism of model probe **CySN-Boc**. b) The emission spectra ($E_x = 635$ nm) of **CySN-NH₃⁺** (10 μ M) in different pH buffers. c) The emission spectra ($E_x = 730$ nm) of **CySN-NH₃⁺** (10 μ M) in different pH buffers. d) The absorption spectra of **CySN-NH₃⁺** (10 μ M) in different pH buffers. e) The PA₆₃₅/PA₇₈₀ of **CySN-NH₃⁺** (50 μ M) in different pH buffers. Inset: the PA signal of **CySN-NH₃⁺** at 635 nm and 780 nm in different pH buffers. Data in e) were expressed as mean \pm s.d. ($n = 3$).

than that of the previously reported platform AS-Cy, demonstrating a reduced channel overlay of CySN platform, especially for the PA channel. Consequently, CySN platform displayed a 603-fold change in NIRF ratio (F_{744}/F_{812}) and a 261-fold change in PA ratio (PA₆₃₅/PA₇₈₀). In comparison with AS-Cy, the ratio changes of CySN platform were enhanced by one to two orders of magnitude, implying significantly improved detection sensitivity for CySN platform. We also employed theoretical calculations to investigate the photophysical properties of AS-Cy and CySN

platform (Figure 3b; Figure S1, Supporting Information). The structures AS-Cy-OAc/AS-Cy-O⁻ and CySN-Boc/CyNS were selected as caged/parent fluorophore for comparison study. It was observed that CySN pair exhibited stronger π -conjugation, with the electron clouds distributed throughout the molecular skeleton, and smaller HOMO-LUMO energy gaps than that of AS-Cy pair, indicating the elongated wavelength of CySN pair. The calculated absorption/fluorescence spectra of CySN pair were also longer than that of AS-Cy pair, suggesting that CySN platform

a

Platform	Fluorescence channel				Photoacoustic channel			
	FL1 (nm)	FL2 (nm)	FL2 - FL1 (nm)	FL ratio change	PA1 (nm)	PA2 (nm)	PA2 - PA1 (nm)	PA ratio change
AS-Cy	733	773	40	10-fold	670	730	60	2.5-fold
CySN	744	812	68	603-fold	635	780	145	261-fold

b

AS-Cy-OAc

AS-Cy-O⁻

CySN-Boc

CyNS

LUMO (-3.13 eV)

LUMO (-2.81 eV)

LUMO (-2.98 eV)

LUMO (-2.71 eV)

HOMO (-5.53 eV)

HOMO (-4.99 eV)

HOMO (-4.99 eV)

HOMO (-4.97 eV)

Energy gap

2.40 eV

2.18 eV

2.01 eV

2.26 eV

Theoretical excitation energy	AS-Cy-OAc	AS-Cy-O ⁻	CySN-Boc	CyNS
FC state (eV)	2.11	1.78	1.67	1.90
Absorption (nm)	589	697	743	652
f_{abs}	1.33	1.30	1.80	1.73
Excited state (eV)	1.67	1.63	1.54	1.64
Emission (nm)	742	760	805	754
f_{em}	1.43	1.49	2.54	2.50

Figure 3. a) The dual-channel NIRF/PA properties of AS-Cy and CySN platforms. b) Computational calculation analysis of probe/product based on AS-Cy and CySN platforms.

is more suitable for deep tissue imaging. The difference in the theoretical de-excitation energy (excited state) between the **CySN** pair is 0.10 eV, which is larger than that of **AS-Cy** pair (0.04 eV), providing a theoretical basis for the reduced channel crosstalk of **CySN**. Moreover, we observed a more significant electron transfer from N atom than S atom in **CySN** pair from HOMO to LUMO, owing to the unequal electron donating ability of N and S. The substantial difference in electron transfer on the donor groups of **CySN** pair may contribute to the smaller crosstalk compared to **AS-Cy** pair.

2.2. Optical Properties of the Dual Ratiometric Probes **CySN-H** and **CySN-E**

Motivated by the results of the model experiment, we proceeded to investigate the versatility of **CySN** as a general platform for constructing activatable probes. We synthesized **CySN-H** probe for hydrogen peroxide and **CySN-E** probe for esterase, representing the detection of small molecule and enzyme biomarkers, respectively (Figure 4a). The detailed synthetic procedure and NMR characterization for these compounds are provided in the supporting information (Scheme S1, Supporting Information). With these probes in hand, we first studied their absorption property changes with and without biomarkers. As shown in Figure 4b,c, with the concentration of H_2O_2 (0 to 100 μM) and esterase (0 to 100 U L^{-1}) increasing, both probes' absorption peak at 780 nm gradually decreased, while the new peak at 635 nm increased consistently. These results were consistent with the model reaction, demonstrating the successful occurrence of the decaging reaction, 1,6-elimination, and Smiles rearrangement. Further HPLC and MS analysis demonstrated the formation of the desired product after incubating the probes with the corresponding analytes (Supporting Information). It is noted that some by-products were identified in the HPLC analysis, which may be attributed to the formation of quinone methide or its Michael addition product with **CyNS**. However, these by-products could potentially be suppressed by the addition of thiol compounds, such as GSH in the cellular environment. Moreover, the use of alternative linkers instead of self-immolative linkers could ameliorate this limitation.

Next, we studied the fluorescence property changes of the probes using a dual fluorescence channel. The time-dependent experiments showed **CySN-H** reached a plateau at \approx 3 hours (with 200 μM H_2O_2), and **CySN-E** reached a plateau at \approx 1 hour (with 100 U L^{-1} esterase) (Figure S2, Supporting Information, $\text{Ex} = 635 \text{ nm}$, $\text{Em} = 744 \text{ nm}$). Furthermore, after reacting with increasing concentrations of biological analytes, the emission peak at 812 nm decreased sharply, while the fluorescent intensity at 744 nm gradually increased (Figure 4d–g). The fluorescent intensity ratio F_{744}/F_{812} of the two probes exhibited an excellent linear relationship with the concentration range (H_2O_2 : 0–20 μM ; esterase: 0–40 U L^{-1}), demonstrating the capability of **CySN** platform of ratiometric sensing different bioanalytes (Figure S3, Supporting Information). The limit of detection (LOD) of ratiometric fluorescence was determined to be 189 nM for **CySN-H** and 0.31 U L^{-1} for **CySN-E**.

We further investigated the PA response of the probes using a dual PA channel. In accordance with the absorption spectrum,

the two probes' PA signals also underwent a blue shift from 780 nm to 635 nm after reacting with H_2O_2 (0–80 μM) and enzyme (0–120 U L^{-1}) (Figure 4h,i). The limit of detection (LOD) of ratiometric PA was determined to be 3.7 μM for **CySN-H** and 6.8 U L^{-1} for **CySN-E** (Figure S4, Supporting Information). These results firmly demonstrated that **CySN-H** and **CySN-E** could efficiently and sensitively detect their targets through dual-channel NIRF/PA modalities.

Next, we evaluated the selectivity of **CySN-H** and **CySN-E** against other biologically interfering reagents. Both probes exhibited significant enhancements in $\text{Abs}_{635}/\text{Abs}_{780}$, F_{744}/F_{812} and $\text{PA}_{635}/\text{PA}_{780}$ towards their desired targets, i.e., H_2O_2 , esterase. In contrast, minimal signal changes were observed when exposed to other interfering compounds, including metal ions, reactive oxygen species, biothiols and other enzymes (Figure 4j–o; Figure S5, Supporting Information). Notably, the F_{744}/F_{812} ratio increased by 395-fold and 367-fold for **CySN-H** and **CySN-E**, respectively, upon interaction with their respective targets. Additionally, the $\text{PA}_{635}/\text{PA}_{780}$ ratios for both probes increased by more than 50-fold. These ratio signal changes were notably higher than those reported for other NIRF/PA probes. These results collectively demonstrate that **CySN-H** and **CySN-E** exhibit outstanding selectivity toward their targets through dual-ratio NIRF/PA detection. In summary, **CySN** showcases its potential as a versatile platform for designing high-performance dual-channel NIRF/PA probes applicable to both small molecules and enzyme analytes.

2.3. NIRF Imaging of **CySN-H** and **CySN-E** in Living Cells

We proceeded to evaluate the cell imaging capabilities of **CySN-H** and **CySN-E**. We first used **CySN-H** to detect exogenous and endogenous H_2O_2 in HeLa cells. For the exogenous H_2O_2 group, cells were incubated with **CySN-H** and then treated with H_2O_2 for another 30 minutes. For the endogenous H_2O_2 group, cells were either incubated with **CySN-H** alone for 30 minutes or co-incubated with phorbol 12-myristate 13-acetate (PMA) for 30 minutes, where PMA was used to stimulate the secretion of H_2O_2 by cells. As illustrated in Figure 5a, **CySN-H** effectively detected both exogenous and endogenous H_2O_2 in HeLa cells through the NIRF channel. The addition of PMA induced a 2.5-fold enhancement in the NIRF channel, comparable to the effect observed with exogenous H_2O_2 (Figure 5b).

Subsequently we investigated the sensing ability of **CySN-E** in live cells. HeLa cells were incubated with **CySN-E**, with or without the pretreatment of esterase inhibitor 4-(2-aminoethyl)benzenesulfonyl fluoride hydrochloride (AEBSF).^[14] The effectiveness of AEBSF in inhibiting esterase activity was firstly confirmed through in vitro experiments (Figure S6, Supporting Information). Cell imaging experiments revealed that the red fluorescence of untreated cells was significantly higher than that of the cells incubated with inhibitors, demonstrating that **CySN-E** effectively detected esterase activity in live cells (Figure S7, Supporting Information). Furthermore, we carried out the ultraviolet radiation study as it can cause cell death and result in the inactivation of esterase.^[15] Specifically, Hela cells were treated with or without UV light for 40 min, followed by a 30 min

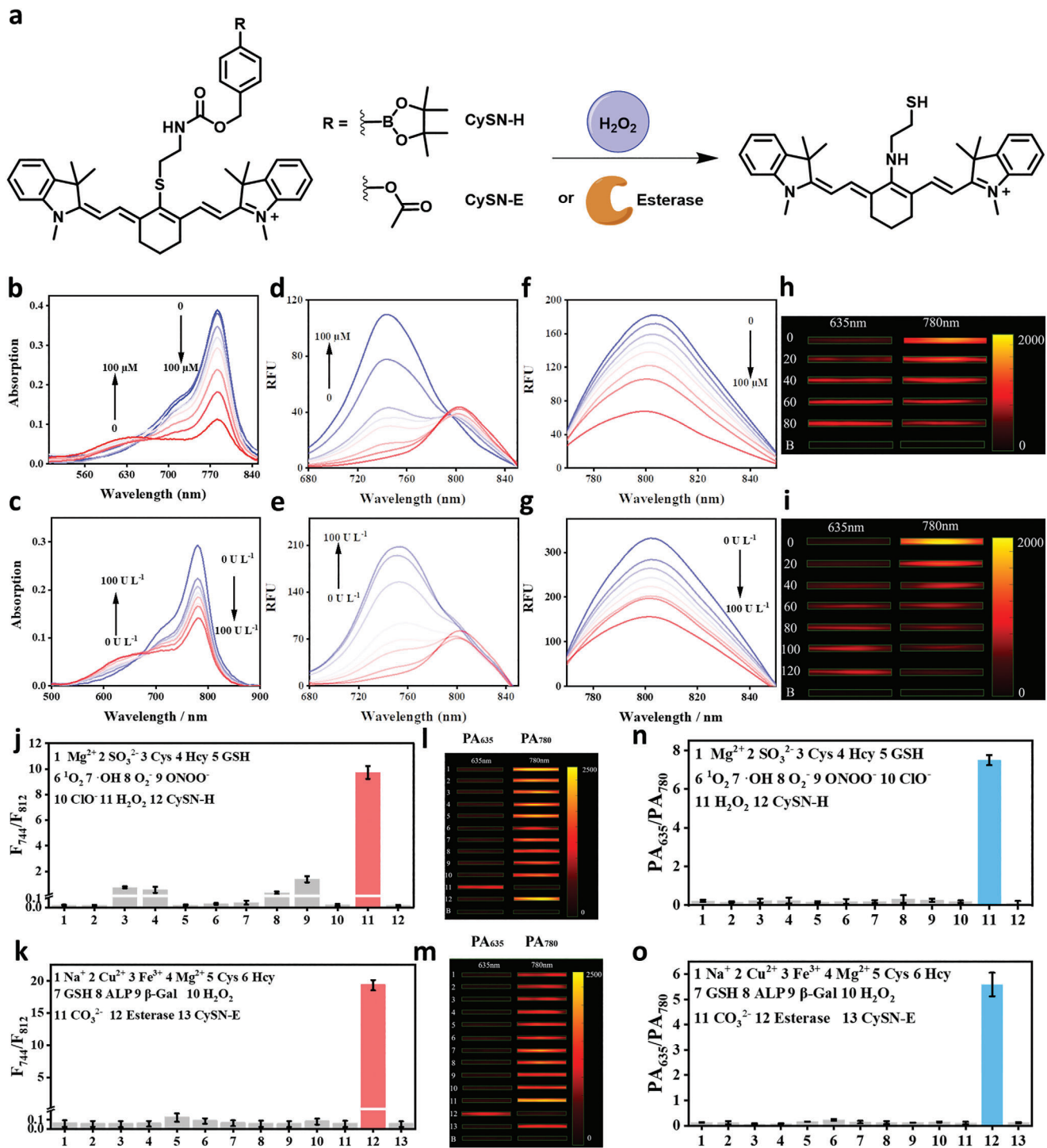


Figure 4. a) Chemical structure and response mechanism of CySN-H and CySN-E. b) The absorption spectra of CySN-H (10 μM) reacted with different concentrations of H_2O_2 (0 to 100 μM) for 2 h. c) The absorption spectra of CySN-E (10 μM) reacted with different concentrations of esterase (0 to 100 U L⁻¹) for 15 min. d, f) Fluorescent spectra of CySN-H (10 μM) reacted with different concentrations of H_2O_2 (0 to 100 μM) for 2 h. (d, excited at 635 nm and f, excited at 730 nm). e,g) Fluorescent spectra of CySN-E (10 μM) reacted with different concentrations of esterase (0 to 100 U L⁻¹) for 15 min. (e, excited at 635 nm and g, excited at 730 nm). h) The PA signal of CySN-H (50 μM) reacted with different concentrations of H_2O_2 (0 to 80 μM) for 2 h. i) The PA signal of CySN-E (50 μM) reacted with different concentration of esterase (0 to 120 U L⁻¹) for 0.5 h. The NIRF ratio (F_{744}/F_{812}) of j) CySN-H (10 μM) or k) CySN-E (10 μM) incubated with various biological interfering reagents. The PA signal of l) CySN-H or m) CySN-E at 635 nm and 780 nm incubated with various biological interfering reagents. The PA ratio (PA_{635}/PA_{780}) (with background subtraction) of n) CySN-H (50 μM) or o) CySN-E (50 μM) incubated with various biological interfering reagents. Data in j,k,n,o) were expressed as mean ± s.d. (n = 3).

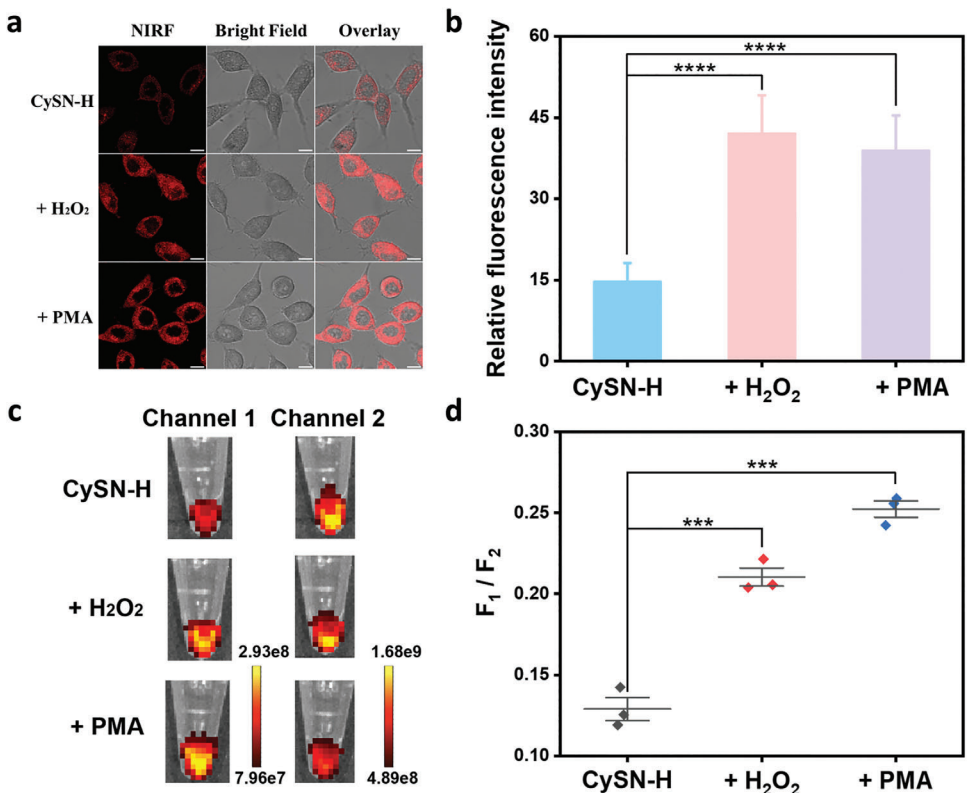


Figure 5. a) The confocal fluorescence images of HeLa cells treated with **CySN-H** (10 μ M), **CySN-H** + H₂O₂ (100 μ M) and **CySN-H** + PMA (10 μ g mL⁻¹). b) Quantitative fluorescence intensity analysis of (a). E_x. 635 nm; E_m. 680 – 780 nm. Scale bar: 10 μ m. c) Ratiometric fluorescence images of HeLa cells pellet with **CySN-H** under various conditions in (a). d) The NIRF ratio (F₁ / F₂) of (c). Channel 1: E_x. 640 nm, filter 710 nm; Channel 2: E_x. 740 nm, filter 790 nm. Data in (b,d) were expressed as mean \pm s.d. ($n = 3$). *** $p < 0.001$, **** $p < 0.0001$.

incubation with **CySN-E**. Cells exposed to UV exhibited significantly lower red fluorescence compared to untreated cells (Figure S8, Supporting Information). The findings indicate that **CySN-E** is a viable method for monitoring cell health by detecting esterase activity.

We further assessed the ratiometric fluorescence imaging capability of our probes, using **CySN-H** as an example. HeLa cell pellets, subjected to the same treatment as the confocal imaging experiments, were collected and imaged using an *in vivo* imaging system. As shown in Figure 5c, the fluorescence emission in channel 2 (E_x. 740 nm, filter 790 nm) observed was notably high in untreated HeLa cells. After adding H₂O₂ or PMA, the fluorescent intensity significantly decreased in channel 2, accompanied by a substantial increase in channel 1 (E_x. 640 nm, filter 710 nm). Furthermore, the calculated fluorescence ratio (F₁/F₂) for HeLa cells treated with H₂O₂/PMA was markedly higher than that of untreated HeLa cells (Figure 5d). These findings robustly demonstrate the NIRF ratiometric imaging capability of our probe in live cells.

2.4. Ratiometric PA Imaging of **CySN-H** and **CySN-E** in Mice Tumor Model

We proceeded to investigate the potential applications of **CySN** based probes in *in vivo* ratiometric PA imaging. The xenograft

4T1 tumor model was established following the previous protocols. Tumors are known to have a relatively high concentration of H₂O₂ in their microenvironment.^[16] The performance of **CySN-H** was initially assessed by subcutaneously injecting it into both the tumor and healthy limbs of mice. As depicted in Figure 6a, in the tumor group, the PA₇₈₀ signal exhibited a clear decrease from 0 to 60 minutes, while the intensity at PA₆₃₅ showed gradual growth. In contrast, the control group displayed no clear changes in either the PA₇₈₀ or PA₆₃₅ channel (Figure 6a). The PA₆₃₅/PA₇₈₀ ratio in the tumor increased significantly, reaching a plateau at 2 hours. And the ratiometric signal was 7-fold higher than that in the normal limb (Figure 6c).

Esterase is overexpressed within cancer cells, playing crucial roles in the growth, invasion and migration of tumors.^[17] We further evaluated the performance of **CySN-E** in a xenograft 4T1 tumor model. Similarly, both the tumor and healthy limbs of mice were subcutaneously injected with **CySN-E**. In the tumor group, the PA signal at 780 nm exhibited a gradual decline, accompanied by an increase in the intensity of PA₆₃₅ (Figure 6b). Conversely, the two PA channels in the normal limbs showed little change over two hours (Figure 6b). The ratio of PA₆₃₅/PA₇₈₀ increased to 1.3 within the tumor group over 2 hours, and the PA ratio in tumor was 3.6 times higher than that in healthy limbs of mice (Figure 6d). It is noteworthy that the tumor-to-normal tissue ratio of the ratiometric PA signal here is much higher than that of **AS-Cy** based probes.

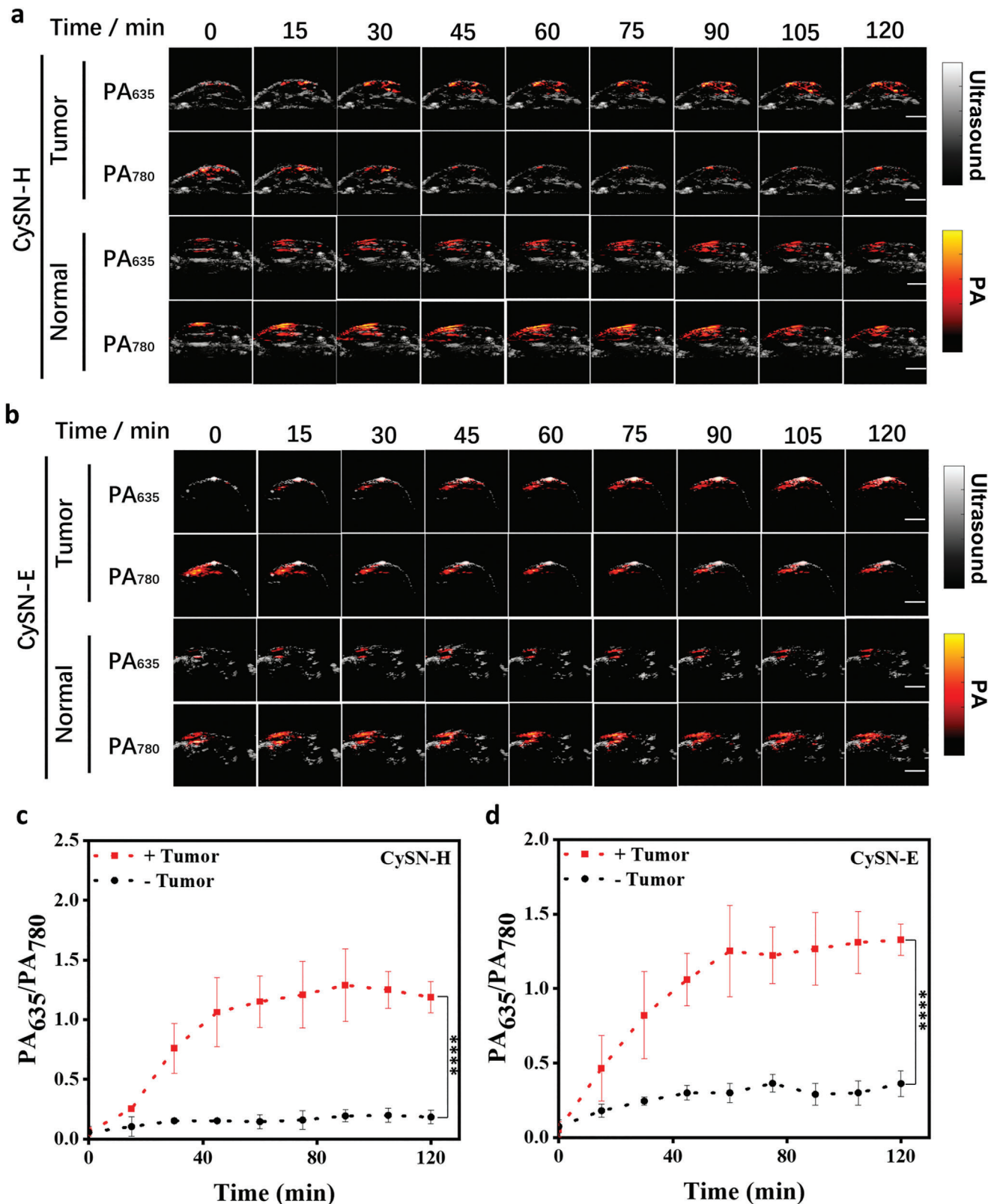


Figure 6. In vivo ratiometric PA images of xenograft 4T1 and normal limbs of mice injected with a) CySN-H and b) CySN-E. c,d) The ratiometric $\text{PA}_{635}/\text{PA}_{780}$ (with background subtraction) change of (a,b). Data in (c,d) were expressed as mean \pm s.d. ($n = 4$). *** $p < 0.0001$. Scale bar: 5 mm.

Furthermore, the ratio of two channel ($\text{PA}_{635}/\text{PA}_{780}$) remained relatively stable when the reaction of **CySN** probes reached saturation within the tumor (Figure 6c,d), whereas the PA signal of ICG (an “always on” reagent with only a single PA channel at 780 nm) decreased over time after injection into the tumor (Figure S9, Supporting Information). This indicated that **CySN**, as a ratiometric platform, might be more suitable for long-term tumor PA imaging compared with ICG dye. The excellent performance of both probes suggests that **CySN-H** and **CySN-E** hold great potential for diagnosing tumors, establishing **CySN** as an outstanding platform for ratiometric PA imaging *in vivo*.

3. Conclusion

In summary, we have established a versatile platform, **CySN**, for designing dual-channel NIRF/PA probes with minimal channel crosstalk and exceptionally large dual-ratiometric signal-to-background ratios. The model experiments demonstrated that **CySN** achieved a remarkable 603-fold change in $\text{F}_{744}/\text{F}_{812}$ and a 261-fold change in $\text{PA}_{635}/\text{PA}_{780}$, representing a significant enhancement compared to the previously reported NIRF/PA probes. Building upon **CySN**, we designed probes **CySN-H** and **CySN-E** for dual-channel NIRF/PA detection of hydrogen peroxide and esterase, respectively. Both probes exhibited high sensitivity and selectivity in *in vitro* experiments. Capitalizing on the advantage of minimal channel overlay in the two ratiometric signals, **CySN** demonstrated excellent performance in PA imaging of living mice, facilitating the detection of both H_2O_2 and esterase activity in tumor models. The ratiometric PA enhancement fold for *in vivo* detection is high and significantly improves the efficiency and accuracy of the probes. We anticipate that the **CySN** platform will stimulate the development of more robust dual-channel NIRF/PA probes for detecting other crucial bioanalytes in disease diagnosis. Furthermore, we envision that our design will inspire further efforts in optimizing optical probes for enhanced performance in clinical applications.

Supporting Information

Supporting Information is available from the Wiley Online Library or from the author.

Acknowledgements

P.W. and Z.Q. contributed equally to this work. The authors thank the financial support from the National Natural Science Excellent Young Scientists Fund of China (Hong Kong and Macau) (Grant No. 32122003), the National Natural Science Foundation of China (NSFC) (81627805, 61805102), and the Research Grants Council of Hong Kong (Grant Nos. 11312422, 11305221, 11103320, 11215817, 11101618).

Conflict of Interest

The authors declare no conflict of interest.

Data Availability Statement

The data that support the findings of this study are available from the corresponding author upon reasonable request.

Keywords

dual-channel platforms, enzymes, fluorescence imaging, high contrast detection, photoacoustic imaging

Received: January 11, 2024

Revised: May 8, 2024

Published online:

- [1] a) S. P. Rowe, M. G. Pomper, *Ca-Cancer J. Clin.* **2022**, *72*, 333; b) L. L. Chen, Y. Lyu, X. Zhang, L. T. Zheng, Q. Q. Li, D. Ding, F. M. Chen, Y. H. Liu, W. Li, Y. T. Zhang, Q. L. Huang, Z. Q. Wang, T. T. Xie, Q. Zhang, Y. Sima, K. Li, S. Xu, T. B. Ren, M. Y. Xiong, Y. Wu, J. B. Song, L. Yuan, H. H. Yang, X. B. Zhang, W. H. Tan, *Sci. China Chem.* **2023**, *66*, 1336.
- [2] a) Y. Wu, S. Huang, J. Wang, L. Sun, F. Zeng, S. Wu, *Nat. Commun.* **2018**, *9*, 3983; b) X. Zhen, J. J. Zhang, J. G. Huang, C. Xie, Q. Q. Miao, K. Y. Pu, *Angew. Chem., Int. Ed.* **2018**, *57*, 7804; c) Q. Li, S. H. Li, S. S. He, W. Chen, P. H. Cheng, Y. Zhang, Q. Q. Miao, K. Y. Pu, *Angew. Chem., Int. Ed.* **2020**, *59*, 7018; d) Y. Q. Zhou, W. Zhang, X. Wang, P. Li, B. Tang, *Chem.-Asian. J.* **2022**, *17*, 202200155.
- [3] a) Y. Zhang, S. He, W. Chen, Y. Liu, X. Zhang, Q. Miao, K. Pu, *Angew. Chem., Int. Ed.* **2021**, *133*, 5986; b) P. Cheng, K. Pu, *Nat. Rev. Mater.* **2021**, *6*, 1095.
- [4] a) J. Huang, K. Pu, *Angew. Chem., Int. Ed.* **2020**, *59*, 11717; b) Y. C. Liu, L. L. Teng, B. L. Yin, H. M. Meng, X. Yin, S. Y. Huan, G. S. Song, X. B. Zhang, *Chem. Rev.* **2022**, *122*, 6850; c) Y. Q. Wang, Y. X. Hu, D. J. Ye, *Angew. Chem., Int. Ed.* **2022**, *61*, 202209512; d) Y. Zhang, G. Zhang, Z. Zeng, K. Pu, *Chem. Soc. Rev.* **2022**, *51*, 566; e) Q. Shen, L. C. Wang, X. H. Ruan, N. Li, W. L. Wang, W. J. Wang, J. J. Shao, X. C. Dong, *Adv. Funct. Mater.* **2023**, *33*, 2300023.
- [5] a) X. L. Huang, J. B. Song, B. C. Yung, X. H. Huang, Y. H. Xiong, X. Y. Chen, *Chem. Soc. Rev.* **2018**, *47*, 2873; b) Z. Xu, X. Huang, X. Han, D. Wu, B. Zhang, Y. Tan, M. Cao, S. H. Liu, J. Yin, J. Yoon, *Chem.* **2018**, *4*, 1609; c) X. Yang, C. C. Li, P. F. Li, Q. R. Fu, *Theranostics* **2023**, *13*, 2632.
- [6] a) L. Yin, H. Sun, H. Zhang, L. He, L. Qiu, J. G. Lin, H. W. Xia, Y. Q. Zhang, S. J. Ji, H. B. Shi, M. Y. Gao, *J. Am. Chem. Soc.* **2019**, *141*, 3265; b) L. Huang, W. Su, L. Zhu, J. Li, W. Quan, J. Yoon, W. Lin, *Angew. Chem., Int. Ed.* **2023**, *135*, 202217508.
- [7] a) Z. Y. Chen, X. L. Mu, Z. Han, S. P. Yang, C. L. Zhang, Z. J. Guo, Y. Bai, W. J. He, *J. Am. Chem. Soc.* **2019**, *141*, 17973; b) J. Zhang, Y. C. Zhang, Q. Guo, G. H. Wen, H. Y. Xiao, S. Qi, Y. Wang, H. T. Zhang, L. D. Wang, H. Y. Sun, *ACS Sens.* **2022**, *7*, 1105; c) Y. Q. Zhang, J. Fang, S. Y. Ye, Y. Zhao, A. N. Wang, Q. L. Mao, C. X. Cui, Y. L. Feng, J. C. Li, S. N. Li, M. Y. Zhang, H. B. Shi, *Nat. Commun.* **2022**, *13*, 1685.
- [8] a) S. He, P. Cheng, K. Pu, *Nat. Biomed. Eng.* **2023**, *7*, 281; b) J. Huang, X. Chen, Y. Jiang, C. Zhang, S. He, H. Wang, K. Pu, *Nat. Mater.* **2022**, *21*, 598.
- [9] a) S. H. Gardner, C. J. Brady, C. Keeton, A. K. Yadav, S. C. Mallojiala, M. Y. Lucero, S. Z. Su, Z. X. Yu, J. S. Hirschi, L. M. Mirica, J. Chan, *Angew. Chem., Int. Ed.* **2021**, *60*, 18860; b) L. Liu, J. Y. Xu, S. P. Zhang, H. Chen, L. P. Wang, X. C. Shen, H. Chen, *Sens. Actuators, B* **2022**, *367*, 132171; c) S. P. Zhang, H. Chen, L. P. Wang, X. Qin, B. P. Jiang, S. C. Ji, X. C. Shen, H. Liang, *Angew. Chem., Int. Ed.* **2022**, *61*, 202107076; d) L. Liu, L. P. Wang, B. S. Tan, X. Q. Wu, H. Chen, X. C. Shen, *Sens. Actuators, B* **2023**, *384*, 133646.
- [10] a) W. Sun, S. G. Guo, C. Hu, J. L. Fan, X. J. Peng, *Chem. Rev.* **2016**, *116*, 7768; b) H. D. Li, D. Kim, Q. C. Yao, H. Y. Ge, J. Chung, J. L. Fan, J. Y. Wang, X. J. Peng, J. Yoon, *Angew. Chem., Int. Ed.* **2021**, *60*, 17268.
- [11] a) C. Vinegoni, I. Botnaru, E. Aikawa, M. A. Calfon, Y. Iwamoto, E. J. Folco, V. Ntziachristos, R. Weissleder, P. Libby, F. A. Jaffer, *Sci. Transl. Actuators, B* **2023**, *384*, 133646.

- Med.* **2011**, *3*, 84ra45; b) Z. H. Hu, C. Fang, B. Li, Z. Y. Zhang, C. G. Cao, M. S. Cai, S. Su, X. W. Sun, X. J. Shi, C. Li, T. J. Zhou, Y. X. Zhang, C. W. Chi, P. He, X. M. Xia, Y. Chen, S. S. Gambhir, Z. Cheng, J. Tian, *Nat. Biomed. Eng.* **2020**, *4*, 259.
- [12] a) R. W. Gao, N. Teraphongphom, E. de Boer, N. S. van den Berg, V. Divi, M. J. Kaplan, N. J. Oberhelman, S. S. Hong, E. Capes, A. D. Colevas, J. M. Warram, E. L. Rosenthal, *Theranostics* **2018**, *8*, 2488; b) D. L. Li, J. J. Zhang, C. W. Chi, X. Xiao, J. M. Wang, L. X. Lang, I. Ali, G. Niu, L. W. Zhang, J. Tian, N. Ji, Z. H. Zhu, X. Y. Chen, *Theranostics* **2018**, *8*, 2508.
- [13] M. C. Caserio, J. K. Kim, *J. Phys. Org. Chem.* **2018**, *31*, e3841.
- [14] J. C. Powers, J. L. Asgian, Ö. D. Ekici, K. E. James, *Chem. Rev.* **2002**, *102*, 4639.
- [15] J. M. Wang, Z. D. Teng, L. Zhang, Y. X. Yang, J. Qian, T. Cao, Y. P. Cao, W. W. Qin, Y. Liu, H. C. Guo, *ACS Sens.* **2020**, *5*, 3264.
- [16] M. López-Lázaro, *Cancer Lett.* **2007**, *252*, 1.
- [17] a) N. S. Qiu, X. R. Liu, Y. Zhong, Z. X. Zhou, Y. Piao, L. Miao, Q. Z. Zhang, J. B. Tang, L. Huang, Y. Q. Shen, *Adv. Mater.* **2016**, *28*, 10613; b) J. B. Zhuang, N. Li, Y. L. Zhang, B. L. Li, H. Q. Wen, X. C. Zhang, T. Y. Zhang, N. Zhao, B. Z. Tang, *CCS Chem* **2022**, *4*, 1028.